

## Poroelastic microlattices for underwater wave focusing

Gunho Kim<sup>a</sup>, Carlos M. Portela<sup>b</sup>, Paolo Celli<sup>c</sup>, Antonio Palermo<sup>d</sup>, Chiara Daraio<sup>a,\*</sup>

<sup>a</sup> Division of Engineering and Applied Science, California Institute of Technology, Pasadena, CA 91125, USA

<sup>b</sup> Department of Mechanical Engineering, Massachusetts Institute of Technology, Cambridge, MA 02139, USA

<sup>c</sup> Department of Civil Engineering, Stony Brook University, Stony Brook, NY 11794, USA

<sup>d</sup> Department of Civil, Chemical, Environmental and Materials Engineering, University of Bologna, 40136 Bologna, Italy



### ARTICLE INFO

#### Article history:

Received 3 June 2021

Received in revised form 21 September 2021

Accepted 1 October 2021

Available online 14 October 2021

#### Keywords:

Microlattices  
Acoustic metamaterials  
Poroelasticity  
Ultrasound  
Wave focusing

### ABSTRACT

Metamaterials with microscale architectures, e.g., microlattices, can exhibit extreme quasi-static mechanical response and tailorable acoustic properties. When coupled with pressure waves in surrounding fluid, the dynamic behavior of microlattices in the long wavelength limit can be explained in the context of Biot's theory of poroelasticity. In this work, we exploit the elastoacoustic wave propagation within 3D-printed polymeric microlattices to incorporate a gradient of refractive index for underwater ultrasonic lensing. Experimentally and numerically derived dispersion curves allow the characterization of acoustic properties of a fluid-saturated elastic lattice. A modified Luneburg lens index profile adapted for underwater wave focusing is demonstrated via the finite element method and immersion testing, showcasing a computationally efficient poroelasticity-based design approach that enables accelerated design of acoustic wave manipulation devices. Our approach can be applied to the design of acoustic metamaterials for biomedical applications featuring focused ultrasound.

© 2021 Published by Elsevier Ltd.

Architected materials consisting of open cell structures with microscale beam elements, i.e., microlattices, can be designed to present desired quasi-static mechanical properties, like low density [1], ultra-low shear modulus [2], or negative Poisson's ratio [3]. In the dynamic regime, the microscopic features found in these materials enable unique responses in the ultrasonic range (above 20 kHz), including wave tunability [4,5], wave focusing [6–8], or amplitude mitigation [9]. When immersed in a viscous fluid, their constitutive properties combined with their porosity lead to an interplay between elastic waves traveling in the microlattices and pressure waves in the surrounding fluid medium [10]. Such interplay leads to complex hybridization phenomena that support exotic responses such as the formation of acoustic band gaps [11] or the strong elasto-acoustic coupling that dominates the fluid's transport properties [12,13]. As such, the selection of specific geometries and structural features allows engineering the propagation of waves in ways that would typically be unachievable with homogeneous or naturally existing materials.

Among various applications of microlattices in the ultrasonic regime, acoustic lensing is of practical importance for its potential use in medical imaging and treatment [14,15]. In particular, by introducing a gradient of refractive index, one can enable focusing of waves with simple manipulation of geometries or materials and without complicated resonant structures [16–19]. Recently,

acoustic gradient-index (GRIN) ultrasonic lenses composed of microlattices have been shown to be capable of focusing plane waves in air [6,7]. This is achieved by controlling the speed of sound by varying the beam thicknesses across the lattice structure. However, this mechanism should be adapted to account for the presence of the fluid and the distortion in the refractive index to work in water. Underwater focusing of ultrasonic waves with microlattice geometry has so far been proposed only with air as a filling agent [8]. However, this approach requires a closed lattice design, which suffers from high impedance mismatch at the lens surface and unwanted hydrostatic pressure differences. A more desirable approach for the design of ultrasonic lenses in underwater conditions relies on fluid-saturated microlattices that account for fluid–structure interaction.

Numerical tools for the design of complex, finite microlattices can be computationally intensive, especially when the lattices are immersed in a fluid. To simplify this process, finite-element representations of fluid-permeated elastic lattices can be replaced by numerical homogenization schemes, which provide an approximation for the expected response. In the low or moderate frequency range, where wavelengths are much larger than the characteristic lengths of the porous medium, the wave propagation characteristics can be effectively estimated via Biot theory [12, 13]. In this long wavelength regime, fluid-filled cellular media can be considered as a homogenized medium characterized by a few effective physical properties, e.g., porosity, tortuosity, etc. [20–23]

In this work, we investigate the characteristics of water-saturated polymeric microlattices in the context of Biot theory

\* Corresponding author.

E-mail address: [daraio@caltech.edu](mailto:daraio@caltech.edu) (C. Daraio).

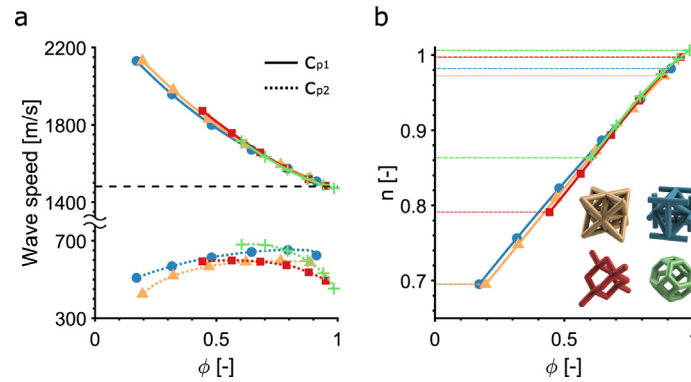


**Fig. 1.** (a) Fast pressure wave speed ( $c_{p1}$ , solid lines) and slow pressure wave speed ( $c_{p2}$ , dotted lines), and (b) effective refractive index ( $n = c_w/c_{p1}$ ) of water-saturated polymeric lattices with respect to porosity for different types of lattices: octet (yellow), isotropic (blue), diamond (red), and Kelvin (green) trusses. The speed of sound in water (1481 m/s) is shown for reference in (a) as the horizontal black dashed line. The excitation frequency of the acoustic wave is fixed at 300 kHz, which is below the estimated viscous Biot frequencies. (For interpretation of the references to color in this figure legend, the reader is referred to the web version of this article.)

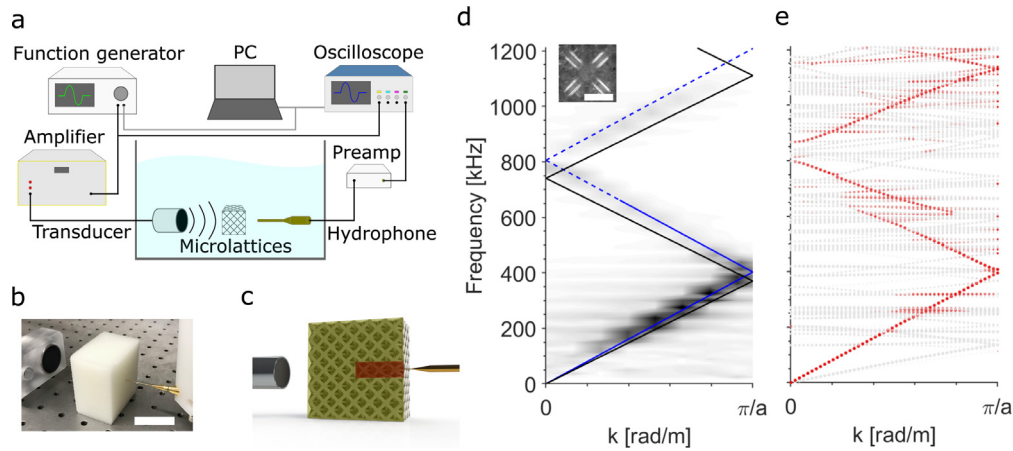
and leverage our findings to realize a fluid-filled GRIN lens. We explore the range of effective refractive index of different types of fluid-saturated microlattices based on continuum theory. We show that the traditional Luneburg lens can be effectively configured as a discretized GRIN lens with modified index profile for underwater wave focusing. We verify our design numerically using a computationally efficient poroelastic model combined with a pressure acoustics study. We validate this design experimentally, by 3D printing a microlattice lens consisting of octet trusses with a spatially varying effective refractive index based on the simulated results. The pressure distribution on the output plane is measured and compared to the numerically estimated pressure intensity field. Both results show good agreement, validating the proposed design approach.

Biot's theory of poroelasticity has been used for the prediction of the macroscopic behavior of acoustic waves traveling through fluid-saturated porous media at low or moderate frequencies [12,13]. According to Biot, the speed and modes of the propagating elastoacoustic waves, which are the products of the coupling between elastic waves in solid and pressure waves in fluid, can be accurately identified. It was analytically predicted [12] and experimentally confirmed [24,25] that the coupled compressional waves split into fast and slow pressure modes in the long wavelength regime. The balance between the boundary layer of Poiseuille flow and the characteristic size of the porous media plays a key role in determining the mode of wave propagation. For a steady, axisymmetric, viscous Poiseuille flow to be established, the boundary layer, also known as the viscous skin depth,  $t_{vis} = \sqrt{2\eta/\omega\rho}$ , must be greater than the radius of the pores of the solid skeleton,  $r$ . Below the 'critical Biot frequency',  $\omega_{crit} = 2\eta/\rho r^2$ , the Poiseuille flow condition holds and the solid and fluid move in phase by viscous locking, which causes the fast compression wave to propagate [12]. Slow pressure waves are not supported, since the relative motion of fluid and solid cannot be sustained. If the forcing frequency exceeds  $\omega_{crit}$ , the Poiseuille flow assumption is no longer valid and the viscous coupling is taken over by inertial coupling, resulting in the occurrence of both fast and slow pressure waves. Slow pressure waves are characterized by the large relative motion between solid and fluid, which makes the waves highly dissipative and difficult to measure experimentally [26]. The inertial coupling is valid below the 'viscous Biot frequency',  $\omega_{vis} = \frac{\omega_{crit}}{\zeta^2}$ , where  $\zeta$  is a non-dimensional scaling constant of the order of 0.01 [27]. For the polymeric microlattices considered in this work, the viscous Biot frequency lies above 317 kHz.

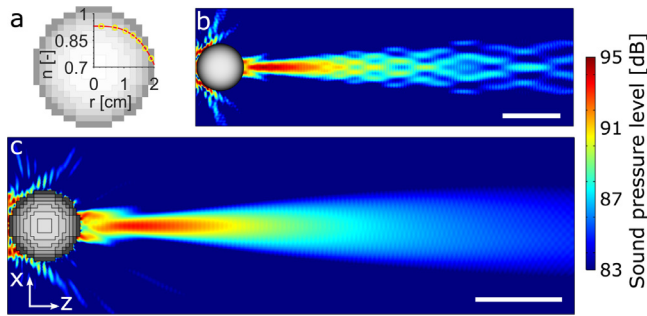
We use finite element models (FEM) (COMSOL<sup>®</sup> Multiphysics) to calculate Biot pressure wave speeds within fluid-saturated microlattices. The homogenized physical parameters for each structure are computed as in Krödel et al. [10]. The characteristic equation of oscillating elastic lattices is numerically solved to obtain the speed of compressional and shear waves,  $c_p$  and  $c_s$ , in the long wavelength limit. The kinetics and kinematics of fluid through the open pores of the microlattices are investigated to calculate the tortuosity,  $\alpha_\infty$ , and permeability,  $\kappa_0$ . These parameters are used as inputs for the coupled characteristic equations of fluid-saturated porous media to derive physical values, such as fast pressure wave speed  $c_{p1}$ , slow pressure wave speed  $c_{p2}$ , and critical Biot frequencies.

Fig. 1 shows the variation of  $c_{p1}$  and  $c_{p2}$ , as well as the corresponding acoustic refractive indices  $n$ , as a function of porosity for four different truss structures, e.g., octet, isotropic, diamond, and Kelvin trusses. The range of porosity is chosen so that the lattice structures are in a manufacturable regime and their topology remains open-celled. The  $c_{p1}$  curves for the four different geometries almost overlap (Fig. 1(a)), whereas the  $c_{p2}$  curves show variations. The speed of the solid-borne waves,  $c_{p1}$ , generally depends on the effective elasticity of the porous media, which is a function of geometry [28]. However, at the manufacturable relative densities for these microlattices, the density-stiffness relation is very similar across architectures [29,30]. Especially when porosity is higher,  $c_{p1}$  is less sensitive to the moduli of the solid and the effect of the bulk modulus of the fluid becomes dominant [31]. Therefore, it is not surprising to observe that  $c_{p1}$  does not vary with the lattice geometry, especially at higher porosity range. On the other hand, the speed of fluid-borne waves,  $c_{p2}$ , depends on the fluid path and on the viscous coupling. Both quantities depend on the tortuosity and the permeability, which are linked to the lattice geometry [31].

The effective acoustic refractive index of a microlattice unit cell is defined as  $n = c_w/c_{p1}$ , where  $c_w$  is the speed of sound in water and  $c_{p1}$  is the speed of fast pressure wave through the porous media. A water-saturated polymeric foam only allows fast compressional waves to propagate due to attenuation of the slow pressure waves [10,32]. In other words, the effective refractive index for different types of polymeric lattices is only a function of  $c_{p1}$ . As such, we expect that variations of refractive index among the different geometries can only be ascribed to their different porosities (Fig. 1(b)). Interestingly, the two bending-dominated lattices reach higher refractive index values, due to their smaller truss connectivity. With higher connectivity, however, the stretch-dominated lattices can achieve larger ranges



**Fig. 2.** (a) Experimental setup with (b) the picture (scale bar: 5 cm) and (c) the 3D model of the measurement system. The model represents the cut plane (yellow) and the drill hole (red) of the test sample. (d) Experimentally reconstructed dispersion curve (gray-scale colormap, normalized between 0 and 1) with the prediction from Biot theory (solid blue line) extrapolated above the viscous critical frequency (dashed blue line). The linear dispersion curve of water wave (black line) is plotted as a reference. (Inset) The microscope image of the unit cell (scale bar: 1 mm). (e) Numerically calculated dispersion relation with longitudinally polarized in-phase modes highlighted in red, others in gray. (For interpretation of the references to color in this figure legend, the reader is referred to the web version of this article.)



**Fig. 3.** (a) Discretized Luneburg lens with continuous (red curve) and discrete (yellow circles) refractive index profiles. Pressure acoustics simulations of Luneburg lens with (b) the continuous profile, and with (c) the discrete layers, with poroelastic properties corresponding to the effective refractive indices selected (scale bar: 5 cm). (For interpretation of the references to color in this figure legend, the reader is referred to the web version of this article.)

of refractive index variation. We can exploit these properties as design features for our acoustic lenses. We choose the octet truss as the fundamental building block for its large refractive index variability (Fig. 1(b)) and the ease of fabrication.

To determine the acoustic characteristics of our samples, we experimentally measure the dispersion relation of water-saturated microlattices and compare the results to a numerically calculated dispersion relation. We fabricate microlattices composed of octet structures using a high-resolution digital light processing (DLP) 3D printing technique (Autodesk® Ember) using PR48™ acrylic photoresist, whose constituent properties are taken to be  $E = 3.3$  GPa,  $\nu = 0.39$ , and  $\rho = 1190$  kg/m<sup>3</sup> [10]. The size of the unit cell is 2 mm along each side with the radius of the truss  $r = 0.16$  mm. To ensure that the wave characteristics are well developed, we allow more than 5 wavelengths along the travel distance, as a rule of thumb. To accommodate 10 wavelengths at 300 kHz, the lowest center frequency of interest, we print 25 cells along the wave propagation direction. To measure the acoustic wave propagation in the fluid saturated lattices, we immerse our structure in water and remove the air trapped in the sample with a vacuum pump. All the measurements are done in a 1.2 m × 0.75 m × 0.75 m water tank surrounded by 2 cm-thick acrylic walls (Precision Acoustics), see Fig. 2(a). The tank is filled with deionized water at room temperature, with negligible variance between measurements. The lattice is positioned between

a broadband ultrasonic transducer (V391-SU, 500 kHz) and a needle hydrophone (Precision Acoustics, 0.2 mm) (Fig. 2(b)). We drill a hole (2 mm wide and 2 cm deep) in the center of the lattice (Fig. 2(c)), to accommodate the insertion of a hydrophone to measure pressure gradients within the sample. Signals are generated by an arbitrary function generator (Keysight Technologies, 33522B) connected to a radio-frequency amplifier (Amplifier Research, 75A220). Hann-windowed 1-cycle sinusoidal pulses are used to excite the lattices, at a central frequency  $f = 300$  kHz. Three single-axis motorized stages (Velmex, BiSlide) are installed above the water tank to control the position of the hydrophone. We measure the transmitted pulse along the drilled hole with constant step increment (0.3 mm), allowing the characterization of the lattice dispersive properties. A pre-amplifier (Precision Acoustics) connected to the hydrophone relays the measured pressure signal to an oscilloscope (Tektronix, DPO 3014). The function generator, the oscilloscope, and the motorized stages are connected to a PC, which enables the integration of signal generation, data acquisition, and positioning functionalities into a single MATLAB code. To reconstruct the dispersion characteristics of our samples, the measured pressure signal is 2D Fourier-transformed into the wavenumber-frequency domain (Fig. 2(d)).

We also investigate the elastoacoustic characteristics via numerical simulations. Finite element models of the fluid-filled microlattices are implemented to derive their dispersion relation. We study the coupled acoustic and stress wave propagation in the [001]-direction under pressure equilibrium and Bloch-Floquet periodic boundary conditions. The acoustic behavior of octet microlattices under an incident plane wave is shown in Fig. 2(e). The strong coupling between structural and acoustic modes results in various hybridized branches. The four main modes are two compressional waves, corresponding to one solid-borne and one fluid-borne pressure waves, and two degenerate shear modes of the elastic frame. We focus on the occurrence of the solid-borne longitudinal modes of the water-saturated polymeric lattices (red dots in Fig. 2(e)), as this mode dominates energy propagation of the ultrasonic waves [32].

The experimental dispersion curve shows a linear, nondispersive response in the frequency range between the critical Biot frequency (61.2 Hz) and the viscous Biot frequency (611.8 kHz), marked by several regions of reduced transmission (Fig. 2(d)). These results agree well with finite-element simulations (Fig. 2(e)), which also show a dispersionless branch (red dotted line in Fig. 2(e)) crossed by localized modes with near zero group

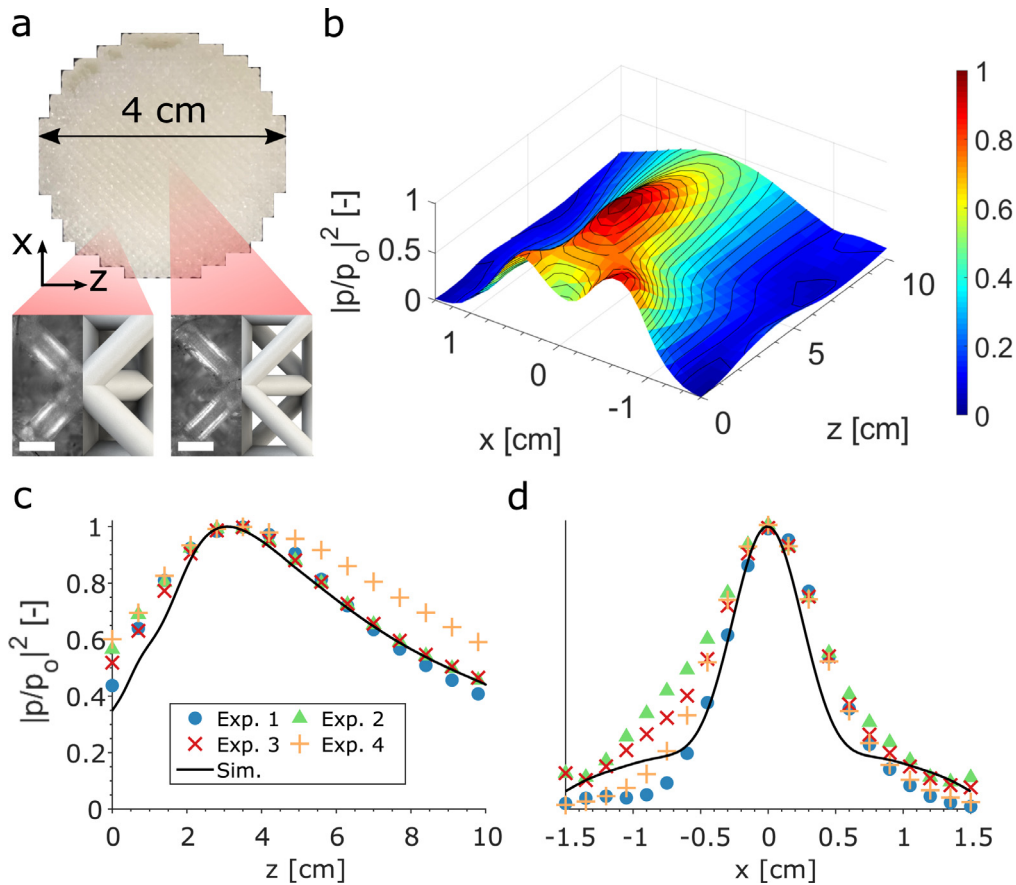


**Fig. 4.** (a) Top-view photograph of the 3D printed Luneburg lens. The insets show optical microscopy images and corresponding models of unit cells from two different regions (scale bar: 0.5 mm). (b) Normalized pressure intensity in the output plane, (c) along the centerline, and (d) across the focal point. Experimental data were measured from four different scan planes along the lens.

velocity. The slope of these branches corresponds to the sound speeds, which are 1641 m/s in the experiments and 1603 m/s in the simulations. A solid-dashed line (blue) overlaid on the experimental dispersion curve corresponds to the fast pressure wave solution of the Biot theory model. The analytical model shows dispersionless mode within an inertia-dominated regime at a constant wave speed of 1611 m/s. We extrapolate the prediction to the frequency region above the viscous critical frequency for a reference. We plot the dispersionless curve of water waves (black) as a reference.

The presence of localized modes, evident in the numerical dispersion curve (e.g., around 300 kHz in Fig. 2(e)), suggests an increased attenuation due to resonances within the microlattices [33]. The localized modes' frequency in the numerical simulations correspond to the region of reduced transmission in the experiments (Fig. 2(d)). However, the regions of reduced transmission are narrow band and do not significantly affect the overall signal transmission. This is evident in Fig. S1, which shows the transmission amplitude as a function of frequency.

At higher frequencies, around 600 kHz, the numerical dispersion curve shows veering of the two fast pressure modes, mixed with multiple localized modes, suggesting the presence of multiple hybridized modes. This manifests as a significant drop in the transmitted amplitude through the lattice at similar frequencies (Fig. 2(d)). A Bragg bandgap is observed in both of the dispersion curves around 800 kHz, which leads to the bending of the branches near the forbidden band. At higher frequencies (above 850 kHz), the dispersion curve shows decreasing group velocity. The dynamic characteristics of the dispersion curve reconstructed

from experiments agree well with the numerical simulations. We exploit these propagation properties to design an acoustic lens.

Based on the dispersion characterization of our water-filled polymeric microlattices, we design a 2D Luneburg lens with a spatially discretized refractive index profile (Fig. 3(a)). In a conventional, continuous GRIN lens, the focal point resides on the lens' surface [34]. However, for most applications, it is useful to place the location of the focal point in a region at a finite distance from the lens surface. To spatially vary the focal distance in water, it is necessary to design an appropriate distribution of the refractive index profile within the lens [35,36]. Moving the focal point outside the lens induces undesirable aberration in the focal region [37]. We minimize these aberrations by further modifying the refractive index distribution within our lens (see Supplementary Material). The original refractive index profile for the Luneburg lens is  $n = \sqrt{2 - r^2/R^2}$ , where  $r$  is the distance from the center of the lens, and  $R$  is the radius of the spherical lens [34]. However, for fluid-saturated polymeric lattices underwater, the refractive index must be smaller than 1 since  $c_{p1}$  is always greater than  $c_w$  (Fig. 2(d)). We introduce a modified Luneburg lens profile,  $n = \sqrt{\frac{1+f^2-(r/R)^a}{bf}}$ , with three nondimensional parameters,  $a = 3.08$ ,  $b = 1.40$ , and  $f = 1.2$  with  $R = 2$  cm. The refractive index distribution of the modified Luneburg lens is shown as a continuous line in Fig. 3(a). The refractive index gradually varies from  $n = 0.93$  at the core of the lens to 0.71 on the outer surface. This profile ensures that the speed of the acoustic waves is larger on the perimeter of the lens than at its center.

To verify our design scheme, we use COMSOL® simulations to compare the pressure acoustic profile of a continuous GRIN lens

(Fig. 3(b)) with our discretized lens (Fig. 3(c)). First, we investigate a continuous Luneburg lens with modified refractive index distribution under incident plane waves at 300 kHz. We model an acoustic domain with  $\rho_w = 1000 \text{ kg/m}^3$  and  $c_w = 1481 \text{ m/s}$  for underwater environment. We define perfectly matched layers (PMLs) around the external boundary of the acoustic domain to minimize unwanted reflections. We plot the sound pressure level of the region of interest with ambient pressure as a reference. The continuous GRIN lens focuses plane waves in a localized region behind the lens (3.15 cm away from the surface).

To validate our discrete lens design, we perform the same finite-element simulation on a lens assembled with different layers of poroelastic media with finite thickness (Fig. 3(c)). A circular Luneburg lens, 4 cm in diameter, consists of total 7 layers of unit cells of  $2 \text{ mm} \times 2 \text{ mm}$  size. We determine the refractive indices of the discretized layers by taking the mean value of the index along the radial direction. Within each layer, we derive the beam thickness of each unit cell from the poroelastic parameters corresponding to the desired refractive index value (Fig. 3(a)).

Both simulations result in similar pressure distributions along the output plane, indicating that the poroelastic model captures effectively the acoustic characteristics of the GRIN lens. The homogenized models of the fluid-saturated lattices are significantly more computationally efficient than the fully discretized simulation with several hundreds of unit cells and solid–fluid interfaces (see Supplementary Material). The pressure distribution in both simulations highlight the presence of scattering and side lobes, resulting in signal transmission loss at the focus.

We 3D print a microlattice-based GRIN lens to validate the lens design experimentally (Fig. 4(a)). The size of each unit cell is 2 mm and the radius of the trusses ranges from 0.15 mm to 0.30 mm, with the thicker beams placed on the outer layers. We excite the lens with Hann-enveloped bursts, consisting of 5 sinusoidal cycles, to achieve narrow bandwidth at the center frequency (300 kHz). To evaluate the focusing, we map the pressure field behind the lens with a 4 mm hydrophone (Fig. 2(a)). We record voltage outputs and normalize them by their peak amplitude. The typical scattered intensity field of the transmitted acoustic waves (Fig. 4(b)) shows the formation of a focal peak ca. 3 cm away from the lens' surface. Side lobes are evident just outside the lens, as predicted in simulations and reported in earlier studies [38].

The results from 4 separate experiments (discrete points) are compared to the numerical predictions (solid black lines), along the directions parallel and perpendicular to the focal point (Fig. 4(c), (d)). The results agree well, with only minor discrepancies among the experimental data arising from the finite height of the 3D printed lens. The focal length, measured from the back of the lens, and the full width at half maximum (FWHM) are evaluated from the results. The focal length of the poroelastic Luneburg lens is observed to be 3 cm, which is in good agreement with the numerical prediction (3.15 cm). We obtain  $3.46(\pm 0.3)\lambda$  for the FWHM of the 3D printed lens whereas the prediction is  $2.8\lambda$ , due to higher amplitudes around the outer edge. The overestimation is caused by the diffraction of the incident wave traveling around the Luneburg lens. In the experiments, the ultrasound emitter has a finite width (unlike the numerical simulations, which assume an incident planar wave front). In addition, the 3D printed lens has a finite height, which increases the diffraction from the top plane. We also ascribe this discrepancy to the limited prediction of the transmission property due to the use of a simplified poroelastic model and due to fabrication errors.

In summary, this work takes advantage of the theory of poroelasticity for the design of underwater Luneburg lenses featuring heterogeneous arrangement of polymeric microlattices filled with

water. We have demonstrated that using poroelastic theory allows for the computationally cheaper and faster design of acoustic wave manipulation devices. This approach could be used for biomedical applications that require focused ultrasound including ultrasonography [39] and sonochemistry [40,41].

## Declaration of competing interest

The authors declare that they have no known competing financial interests or personal relationships that could have appeared to influence the work reported in this paper.

## Acknowledgments

This work was supported by the Rosen Center for Bioengineering, USA. Gunho Kim was funded by the Kwanjeong Educational Foundation, South Korea. GK and CD thank the founders of the Rosen center, Donna and Benjamin M. Rosen, and the president of Kwanjeong Foundation, Chonghwan Lee, for their vision and support. AP, PC and GK thank Daniel Marti Dafcik for his support during the earliest stages of this project.

## Appendix A. Supplementary data

Supplementary material related to this article can be found online at <https://doi.org/10.1016/j.eml.2021.101499>.

## References

- [1] T.A. Schaedler, A.J. Jacobsen, A. Torrents, A.E. Sorensen, J. Lian, J.R. Greer, L. Valdevit, W.B. Carter, Ultralight metallic microlattices, *Science* 334 (6058) (2011) 962–965.
- [2] M. Kadic, T. Bückmann, N. Stenger, M. Thiel, M. Wegener, On the practicality of pentamode mechanical metamaterials, *Appl. Phys. Lett.* 100 (19) (2012) 191901.
- [3] T. Bückmann, N. Stenger, M. Kadic, J. Kaschke, A. Frölich, T. Kennerknecht, C. Eberl, M. Thiel, M. Wegener, Tailored 3D mechanical metamaterials made by dip-in direct-laser-writing optical lithography, *Adv. Mater.* 24 (20) (2012) 2710–2714.
- [4] X. Xia, A. Afshar, H. Yang, C.M. Portela, D.M. Kochmann, C.V. Di Leo, J.R. Greer, Electrochemically reconfigurable architected materials, *Nature* 573 (7773) (2019) 205–213.
- [5] E.L. Walker, D. Reyes-Contreras, Y. Jin, A. Neogi, Tunable hybrid phononic crystal lens using thermo-acoustic polymers, *ACS Omega* 4 (15) (2019) 16585–16590.
- [6] L. Zigoneanu, B.-I. Popa, S.A. Cummer, Design and measurements of a broadband two-dimensional acoustic lens, *Phys. Rev. B* 84 (2011) 024305.
- [7] Y. Xie, Y. Fu, Z. Jia, J. Li, C. Shen, Y. Xu, H. Chen, S.A. Cummer, Acoustic imaging with metamaterial Luneburg lenses, *Sci. Rep.* 8 (1) (2018) 1–6.
- [8] A. Allam, K. Sabra, A. Erturk, 3D-printed gradient-index phononic crystal lens for underwater acoustic wave focusing, *Phys. Rev. Appl.* 13 (2020) 064064.
- [9] A. Krusová, M. Sevcík, H. Seiner, P. Sedláč, B. Román-Manso, P. Miranzo, M. Belmonte, M. Landa, Ultrasonic bandgaps in 3D-printed periodic ceramic microlattices, *Ultrasonics* 82 (2018) 91–100.
- [10] S. Krödel, A. Palermo, C. Daraio, Acoustic properties of porous microlattices from effective medium to scattering dominated regimes, *J. Acoust. Soc. Am.* 144 (1) (2018) 319–329.
- [11] S. Krödel, C. Daraio, Microlattice metamaterials for tailoring ultrasonic transmission with elastoacoustic hybridization, *Phys. Rev. A* 6 (6) (2016) 1–9.
- [12] M.A. Biot, Theory of propagation of elastic waves in a fluid-saturated porous solid. I. Low-frequency range, *J. Acoust. Soc. Am.* 28 (2) (1956) 168–178.
- [13] M. Biot, Theory of propagation of elastic waves in a fluid-saturated porous solid. II. Higher frequency range, *J. Acoust. Soc. Am.* 28 (2) (1956) 179–191.
- [14] R.V. Craster, S. Guenneau, *Acoustic Metamaterials*, Springer, 2012.
- [15] N. McDannold, N. Vykhodtseva, K. Hynynen, Blood-brain barrier disruption induced by focused ultrasound and circulating preformed microbubbles appears to be characterized by the mechanical index, *Ultrasound* 34 (5) (2009) 834–840.
- [16] S.-C.S. Lin, T.J. Huang, J.-H. Sun, T.-T. Wu, Gradient-index phononic crystals, *Phys. Rev. B* 79 (2009) 094302.

- [17] T.P. Martin, M. Nicholas, G.J. Orris, L.-W. Cai, D. Torrent, J. Sánchez-Dehesa, Sonic gradient index lens for aqueous applications, *Appl. Phys. Lett.* 97 (11) (2010) 113503.
- [18] S. Peng, Z. He, H. Jia, A. Zhang, C. Qiu, M. Ke, Z. Liu, Acoustic far-field focusing effect for two-dimensional graded negative refractive-index sonic crystals, *Appl. Phys. Lett.* 96 (26) (2010) 263502.
- [19] Y. Ye, M. Ke, Y. Li, T. Wang, Z. Liu, Focusing of spoof surface-acoustic-waves by a gradient-index structure, *J. Appl. Phys.* 114 (15) (2013) 154504.
- [20] J. Allard, N. Atalla, *Propagation of Sound in Porous Media: Modelling Sound Absorbing Materials 2e*, John Wiley & Sons, 2009.
- [21] M.A. Biot, D. Willis, The elastic coefficients of the theory of consolidation, *J. Appl. Mech.* 24 (1957) 594–601.
- [22] J.G. Berryman, Origin of Gassmann's equations, *Geophysics* 64 (5) (1999) 1627–1629.
- [23] P.C. Johnson, R. Jackson, Frictional-collisional constitutive relations for granular materials, with application to plane shearing, *J. Fluid Mech.* 176 (1987) 67–93.
- [24] T.J. Plona, Observation of a second bulk compressional wave in a porous medium at ultrasonic frequencies, *Appl. Phys. Lett.* 36 (4) (1980) 259–261.
- [25] J.G. Berryman, Confirmation of Biot's theory, *Appl. Phys. Lett.* 37 (4) (1980) 382–384.
- [26] O. Kelder, D.M.J. Smeulders, Observation of the Biot slow wave in water-saturated Nivelsteiner sandstone, *Geophysics* 62 (6) (1997) 1794–1796.
- [27] E.R. Hughes, T.G. Leighton, G.W. Petley, P.R. White, R.C. Chivers, Estimation of critical and viscous frequencies for Biot theory in cancellous bone, *Ultrasonics* 41 (5) (2003) 365–368.
- [28] J.G. Berryman, Elastic wave propagation in fluid-saturated porous media, *J. Acoust. Soc. Am.* 69 (2) (1981) 416–424.
- [29] L.R. Meza, G.P. Philipot, C.M. Portela, A. Maggi, L.C. Montemayor, A. Comella, D.M. Kochmann, J.R. Greer, Reexamining the mechanical property space of three-dimensional lattice architectures, *Acta Mater.* 140 (2017) 424–432.
- [30] C.M. Portela, J.R. Greer, D.M. Kochmann, Impact of node geometry on the effective stiffness of non-slender three-dimensional truss lattice architectures, *Extrem. Mech. Lett.* 22 (2018) 138–148.
- [31] B.B.S.A. Vogelaar, *Fluid Effect on Wave Propagation in Heterogeneous Porous Media* (Ph.D. thesis), Technische Universiteit Delft, 2009.
- [32] J.F. Allard, C. Depollier, A. L'Esperance, Observation of the Biot slow wave in a plastic foam of high flow resistance at acoustical frequencies, *J. Appl. Phys.* 59 (10) (1986) 3367–3370.
- [33] G. Ma, P. Sheng, Acoustic metamaterials: From local resonances to broad horizons, *Sci. Adv.* 2 (2) (2016) e1501595.
- [34] R.K. Luneburg, *Mathematical Theory of Optics*, University of California Press, 1944.
- [35] S.P. Morgan, General solution of the Luneberg lens problem, *J. Appl. Phys.* 29 (9) (1958) 1358–1368.
- [36] A. Gutman, Modified Luneberg lens, *J. Appl. Phys.* 25 (7) (1954) 855–859.
- [37] W. Jagger, The optics of the spherical fish lens, *Vis. Res.* 32 (7) (1992) 1271–1284.
- [38] N. Mohammadi Estakhri, A. Alù, Wave-front transformation with gradient metasurfaces, *Phys. Rev. X* 6 (2016) 041008.
- [39] J.M. Sanches, A.F. Laine, J.S. Suri, *Ultrasound Imaging*, Springer, 2012.
- [40] K.S. Suslick, Sonochemistry, *Science* 247 (4949) (1990) 1439–1445.
- [41] K. Yasui, Fundamentals of acoustic cavitation and sonochemistry, in: M. Ashokkumar (Ed.), *Theoretical and Experimental Sonochemistry Involving Inorganic Systems*, Springer Netherlands, Dordrecht, 2011, pp. 1–29.